# Creep behaviour and microstructural stability of cast nickel based superalloy IN 792 5A

J. Hakl[1*] , T. Vlasák[1], J. Lapin[2]

[1] *SVÚM, a.s., Podnikatelská 565, 190 11 Prague 9, Czech Republic*
[2] *Institute of Materials and Machine Mechanics, Slovak Academy of Sciences, Račianska 75, 831 02 Bratislava, Slovak Republic*

Received 31 May 2007, received in revised form 11 July 2007, accepted 11 July 2007

**Abstract**

Creep behaviour and long-term microstructural stability of cast nickel based superalloy IN 792 5A were studied. This investment cast superalloy fully fulfils current requirements of gas turbine designers of turbine blades and other hot parts of gas turbines and turbochargers. The methodology for evaluation creep characteristics and measured creep properties such as creep strength, creep strength to 1 % strain and minimum creep rates are presented. The microstructure analysis of specimens before and after creep testing showed that the initial microstructure is unstable during long-term creep exposure. Coarsening of cuboidal $\gamma'$ precipitates and the development of rafted structure in some equiaxed grains are quantitatively analysed. The alloy fails by growth and coalescence of cavities and cracks formed at the grain boundaries, interfaces between eutectic regions and the $\gamma/\gamma'$ matrix and within brittle carbide particles.

K e y w o r d s: Ni based superalloy, castings, creep properties, microstructure

## 1. Introduction

Nickel based superalloys have been developed for processing of specific components operating at high temperatures and complex stresses in stationary gas turbines, aircraft engines and automotive turbochargers. The main requirements on these materials are: (i) resistance against complex damage mechanisms during mechanical loading at high temperatures, (ii) resistance against corrosive effects of hot gases and (iii) optimized balance of mechanical and technological properties for specific processing routes such as hot rolling, forging and casting. Due to strategic importance of nickel based superalloys, particularly in the aircraft industry, superalloys have become one of the most studied group of metallic materials [1–7]. Relatively frequently used superalloys including examples of their applications by world leading manufacturers were recently reviewed by several authors [8–12]. It should be noted that the nickel based superalloys of the last generation still offer higher room temperature ductility, fracture toughness and superior combination of high temperature mechanical properties when compared to multiphase nickel based intermetallics [13, 14]. On the other hand, at intermediate temperatures ranging from about 650 to 750 ℃, nowadays nickel based superalloys have to compete with emerging group of titanium based intermetallics with significantly lower density (about 4 g $cm^{-3}$) and comparable or superior specific strength [15–19] and cheaper iron based aluminides [20–23].

IN 792 belongs to the second generation of nickel based superalloy and it has been used industrially since the 1970s. The IN 792 superalloy is complexly alloyed material designed for investment casting. Mechanical properties of this alloy can be optimized through appropriate heat treatments including solution and precipitation annealing. The IN 792 is produced in several modifications which differ slightly in their chemical composition. Besides 5A modification, which is probably the most popular, more expensive 5B and 5C variants contain also 0.5 and 0.9 (wt.%) of hafnium, respectively [24]. Nominal chemical composition of IN 792 5A and reference nickel based superal-

*Corresponding author: tel.: +420 274023132; fax: +420 222729256; e-mail address: hightempmat@svum.cz

Table 1. Nominal chemical composition of nickel based superalloys IN 713 LC, IN 738 LC and IN 792 5A (in wt.%)

| Alloy | C | Cr | Co | Mo | W | Nb | Ta | Ti | Al | Zr | B |
|---|---|---|---|---|---|---|---|---|---|---|---|
| IN 713 LC | 0.05 | 12.0 | – | 4.50 | – | 2.00 | – | 0.60 | 5.90 | 0.10 | 0.010 |
| IN 738 LC | 0.10 | 16.0 | 8.5 | 1.75 | 2.60 | 0.85 | 1.75 | 3.40 | 3.40 | 0.05 | 0.010 |
| IN 792 5A | 0.08 | 12.5 | 9.0 | 1.90 | 4.17 | – | 4.17 | 3.97 | 3.37 | 0.03 | 0.015 |

loys IN 713 LC and IN 738 LC are shown in Table 1.

Basic creep properties of the IN 792 alloy have been already published [25] but this information is limited when compared to other nickel based superalloys. On the other hand, the data about creep properties of IN 792 5A superalloy are still lacking in available literature. It should be noted that our research on creep behaviour of IN 792 5A alloy was motivated by the industry that selected this system for specific structural applications at high temperatures.

The aim of this paper is to study creep behaviour and the effect of creep exposure on the microstructure stability of cast nickel based superalloy IN 792 5A.

## 2. Experimental procedure

Conical ingots with minimum diameter of 13 mm, maximum diameter of 18 mm and length of 90 mm were cast by a foundry company PBS Velká Bíteš from a master alloy supplied by Ross and Catherall. After casting the ingots were subjected to two-step annealing at 1120 ℃ for 2 h followed by air cooling and at 845 ℃ for 24 h finalized by air cooling. The analysed chemical composition of the ingots is given in Table 2.

Cylindrical creep specimens (48 pieces) with gauge diameter of 5 mm and gauge length of 50 mm and threaded heads of M12 × 15 mm were lathe machined from the heat treated castings. The constant load creep tests were performed at applied stresses ranging from 80 to 540 MPa at temperatures from 750 to 975 ℃. The creep experiments were done at testing laboratory accredited according to certificate ČSN EN ISO/IEC 17025:2005 at SVÚM Prague. Control of creep temperature accuracy was according to the ČSN EN 10291 standard, e.g. accuracy of ±4 ℃ and ±6 ℃ for the temperature ranges from 600 to 800 ℃ and from 800 to 1000 ℃, respectively. Elongation of creep specimens was measured by extensometers with 10 $\mu$m resolution.

The microstructure analysis of specimens before and after creep testing was performed by light optical microscopy (LOM), scanning electron microscopy (SEM) and energy-dispersive X-ray spectroscopy. LOM and SEM samples were prepared using standard metallographic techniques including grinding at abrasive papers and mechanical polishing on diamond pastes up to 1 $\mu$m. After polishing the samples were etched in a reagent of 25 ml of ethanol, 25 ml $HNO_3$ and 26 ml HCl. The size and volume fraction of precipitates were determined by computerized image analysis. For this purpose, statistical number of digitalized SEM micrographs (20 photos) was taken for selected creep regimes.

Table 2. Measured chemical composition of cast ingots (in wt.%) and calculated electron vacancy number $\mu N_V$

| Element | Specification | | Heat Analysis |
|---|---|---|---|
| | min | max | |
| C | 0.060 | 0.100 | 0.078 |
| Cr | 12.00 | 13.00 | 12.28 |
| Mo | 1.65 | 2.15 | 1.81 |
| Nb | – | 0.50 | < 0.10 |
| Ta | 3.85 | 4.50 | 4.12 |
| Al | 3.15 | 3.60 | 3.36 |
| Ti | 3.75 | 4.20 | 3.98 |
| B | 0.010 | 0.020 | 0.015 |
| Zr | 0.010 | 0.050 | 0.031 |
| Si | – | 0.20 | < 0.10 |
| Mn | – | 0.15 | < 0.10 |
| Fe | – | 0.50 | 0.16 |
| Co | 8.50 | 9.50 | 8.87 |
| W | 3.85 | 4.50 | 4.10 |
| S | – | 0.015 | < 0.002 |
| P | – | 0.015 | < 0.002 |
| $\mu N_V$ | – | – | 2.26 |

## 3. Results

### 3.1. Sensitivity of IN 792 5A alloy to $\sigma$ phase formation

Because of the complex alloying, the IN 792 5A alloy has a tendency to form undesirable $\sigma$ phase when exposed to high temperatures. The $\sigma$ phase is an intermetallic, topologically closely packed phase which exists especially in plate or needle-like morphology. This phase can precipitate at the studied temperature interval from 650 to 950 ℃, particularly during creep loading. The tendency of nickel based superalloys to form the $\sigma$ phase can be predicted from their chemical composition using well-known PHACOMP (acronym for Phase Computation) method [26]. Many modifications of this method, which differ in computation procedure, can be found in literature [27, 28].

Table 3. Calculation of electron vacancy number

| Step | Description |
|---|---|
| 1 | Convert the composition from weight per cent to atomic per cent. |
| 2 | Assumption for calculation of phase composition: One half of the C forms MC carbides, remaining C forms $M_{23}C_6$ carbides |
| | All B is combined as $Mo_3B_2$ |
| | The $\gamma'$ is $Ni_3$(Al, Ti, Ta, Nb) |
| 3 | The residual matrix will consist of the atomic per cent minus those atoms combined in the carbide, boride and $\gamma'$. |
| 4 | Conversion of this on a 100% basis which gives in atomic per cent of each element remaining in the matrix |
| 5 | Formula for calculation of the electron vacancy number is as follows: $\mu N_v = 0.66\text{Ni} + 1.71\text{Co} + 2.66\text{Fe} + 3.66\text{Mn} + 4.66(\text{Cr} + \text{Mo} + \text{W}) + 5.66\text{V} + 0.66(\text{Si} + \text{Zr})$ |

Table 4. Size of primary and secondary cuboidal $\gamma'$ precipitates, width of $\gamma$ channels, width of $\gamma'$ rafts and length of $\gamma'$ rafts

| State | Size of primary $\gamma'$ precipitates (nm) | Size of secondary $\gamma'$ precipitates (nm) | Width of $\gamma$ channels (nm) | Width of $\gamma'$ rafts (nm) | Length of $\gamma'$ rafts (nm) |
|---|---|---|---|---|---|
| Before creep | 480 | 115 | 57 | – | – |
| Creep 850 °C/240 MPa | 530 | 250 | 240 | 540 | 690 |
| Creep 950 °C/80 MPa | 705 | – | 540 | 720 | 1950 |

The basic assumption for PHACOMP method is that the $\sigma$ phase is an electron compound and its occurrence is conditioned by a certain number of vacant places in the electron envelope (so called electron vacancies) of the elements which form a solid solution. The computation then involves determining

$$\mu N_V = \sum_i m_i N_{Vi}, \quad (1)$$

where $\mu N_V$ is the mean value of electron vacancies of the elements which form the solid solution, $m_i$ is an atomic fraction of $i$-th element of the solid solution and $N_{Vi}$ is the number of electron vacancies in electron envelopes of $i$-th element.

Criterion for the composition's suitability is defined as

$$\mu N_V \leq N_{Vkrit}, \quad (2)$$

where $N_{Vkrit}$ is the critical value of $\mu N_V$ (material constant). The alloy is not predisposed to form the $\sigma$ phase when Eq. (2) is fulfilled. The PHACOMP method used in this work is based on several simplifications and individual steps of these calculations are schematically shown in Table 3. Applying this procedure for the studied IN 792 5A alloy results in electron vacancy of $\mu N_V = 2.26$ (see Table 2), which is lower than the critical value of $N_{Vkrit} = 2.38$ [24]. These calculations suggest that the $\sigma$ phase should not be formed during long-term high temperature exposure of IN 792 5A. It should be noted that the full procedure adopted for computer calculation of electron vacancies is described in [29].

### 3.2. Microstructure before creep

The microstructure of the as-cast and heat treated nickel-based superalloy IN 792 5A alloy consisted of equiaxed grains with a mean grain diameter of 650 $\mu$m. Figure 1 shows the typical microstructure within the grains. Besides the typical cuboidal $Ni_3$(Al,Ti) precipitates ($\gamma'$ phase) in the $\gamma$ matrix (Ni-based solid solution), the microstructure contains needle-like precipitates, which were identified by energy dispersive spectroscopy to be carbides, as shown in Fig. 1a. In some regions, formation of $\gamma/\gamma'$ eutectic (E) was observed, as shown in Fig. 1b. The eutectic regions are usually surrounded with a layer (L) containing fine $\gamma'$ precipitates in the $\gamma$ matrix and carbide particles. As illustrated in Fig. 1c, two-step ageing at 1120 °C/2 h and

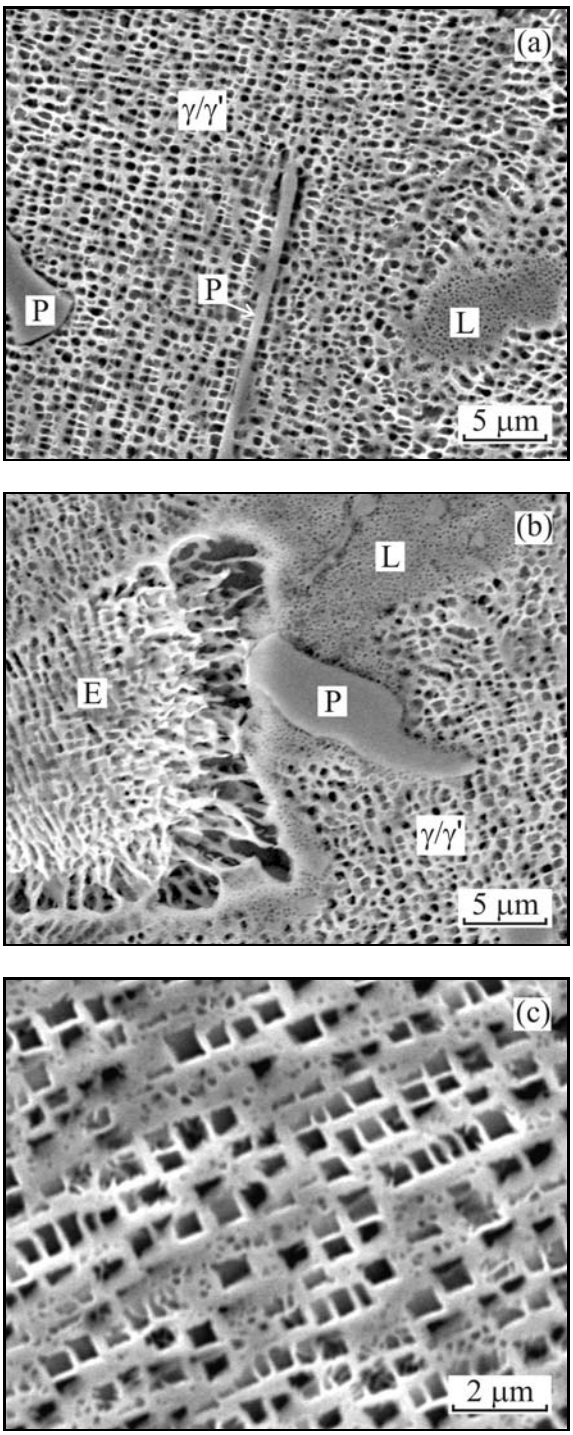


Fig. 1. SEM micrographs showing microstructure of IN 792 5A alloy before creep testing: (a) the typical $\gamma/\gamma'$ microstructure with needle-like carbide particles; (b) $\gamma/\gamma'$ eutectic region with carbide particle; (c) primary (larger) and secondary (smaller) $\gamma'$ precipitates in the $\gamma$ matrix. P – carbide particle, E – eutectic region, L – layer with fine $\gamma/\gamma'$ type of microstructure.

845 ℃/24 h leads to a bimodal size of the $\gamma'$ precipitates. Figure 2 shows a distribution curve for the measured size $d$ (edge length) of cuboidal $\gamma'$ precipitates. The distribution curve clearly indicates two peaks corresponding to primary and secondary $\gamma'$ particles with a mean size of $d_p = 480$ nm and $d_s = 115$ nm, respectively. Volume fraction of $\gamma'$ precipitates was measured to be 68 ± 4 vol.%. Besides the size and volume fraction of strengthening particles, an important structural parameter affecting the creep strength of the studied alloy is the width of $\gamma$ channels separating cuboidal $\gamma'$ particles. All measured values of width of $\gamma$ channels were fitted by log-normal distribution function, as seen in Fig. 3. Table 4 summarizes statistically determined mean values of the $\gamma'$ precipitate size and width of $\gamma$ channels. It should be noted that the mean values were determined from about 1700 statistical measurements for each microstructural parameter.

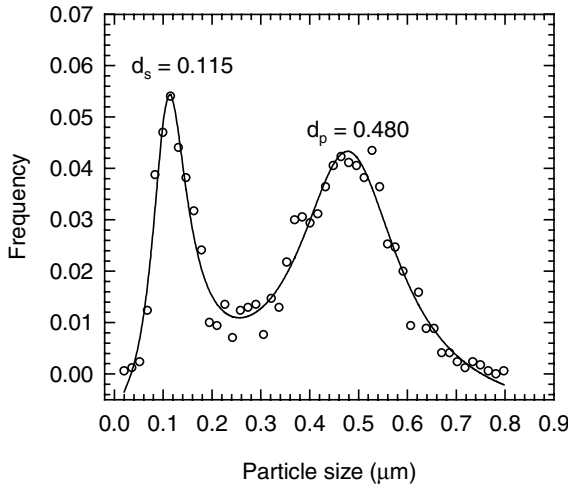


Fig. 2. Bimodal distribution of $\gamma'$ particle size before creep testing.

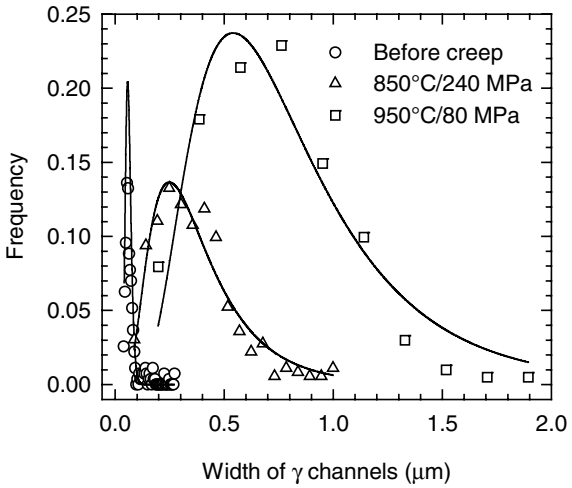


Fig. 3. Log-normal distribution curves of measured width of $\gamma$ channels.

### 3.3. Creep

#### 3.3.1. Assessment methodology of creep characteristics

In order to assess the time to rupture as a function of temperature and applied stress $\sigma$, the relation defined in [30] was used in the form

$$\log \sigma = A_1 + A_2 P_{\mathrm{LM}} + A_3 P_{\mathrm{LM}}^2, \tag{3}$$

where $A_1$, $A_2$ and $A_3$ are material constants and $P_{\mathrm{LM}}$ is the Larson-Miller parameter defined as

$$P_{\mathrm{LM}} = T(\log t_{\mathrm{r}} + A_4), \tag{4}$$

where $T$ is the absolute temperature, $t_{\mathrm{r}}$ is the time to rupture and $A_4$ is a material constant. Linear material constants were estimated using the least square method, non-linear constants were determined by gradual iteration [31]. This method was used in all following cases of determining material constants.

In order to determine creep deformation characteristics, firstly individual creep curves were evaluated. Figure 4 shows creep deformation curves at temperatures ranging from 800 to 950 °C. Total creep deformation $\varepsilon_{\mathrm{c}}$ as a function of time, characterized by limiting deformation $\varepsilon_{\mathrm{m}}$ and initial deformation $\varepsilon_0$, can be in all three stages of creep described by means of model in the form [32, 33]

$$\varepsilon_{\mathrm{c}} = \varepsilon_0 \cdot \left[ \left[ \frac{\varepsilon_{\mathrm{m}}}{\varepsilon_0} \right]^{[g(\pi(t))]} - 1 \right], \tag{5}$$

where $t$ is the time. The time-dependent function of integral intensity of the creep process $g(\pi(t))$ is defined by the following relation

$$g\left(\pi(t)\right) = \pi^N \left[ \frac{1 + \exp\left(-2\pi^K\right)}{1 + \exp\left(-2\right)} \right]^M, \tag{6a}$$

where $K$, $M$ and $N$ are material constants and $g$ is a function of damage parameter $\pi(t)$ in a normalized form

$$\pi = \frac{t}{t_{\mathrm{r}}}. \tag{6b}$$

The initial elastic deformation $\varepsilon_0$ is controlled by the Hooke's law

$$\varepsilon_0 = \frac{\sigma}{E(T)} 10^2, \tag{6c}$$

where $E(T)$ is the temperature dependence of the Young's modulus. The following form was used to determine the module of elasticity as a function of temperature

$$E(T) = E_1 + E_2 \exp\left(\frac{E_3}{T}\right), \tag{6d}$$

where $E_1$, $E_2$ and $E_3$ are material constants. Limiting deformation $\varepsilon_{\mathrm{m}}$ is a quantity of deformation determined by extrapolating of creep curve between the point shortly before failure, when deformation increases extremely fast, and the point of failure. The time interval of the very fast deformation acceleration constitutes of about 1 % of the overall time to failure. Thus non-inclusion of the stage of collapse before failure into the mathematical description is a simplification which has a minimum impact on the description of the creep process. In addition, it is a stage of the creep process which is totally insignificant from the application point of view. The scope of the experiments did not allow evaluation of the limited deformation $\varepsilon_{\mathrm{m}}$ as a function of the time to failure and temperature. However, for the description of individual creep curves, this parameter can be considered to be a material constant.

Mathematical description of the creep curves allows to determine other creep characteristics. The first of these is the strength for specific creep strain. From Eqs. (6a) to (6d), one can obtain for each curve the time when the selected deformation (e.g. 1 %) is reached. In order to determine the creep strength for 1 % strain as a function of temperature and stress, a regression model formally identical to Eq. (5) was used

$$\log \sigma_1 = B_1 + B_2 \cdot P_{\mathrm{LM}} + B_3 \cdot P_{\mathrm{LM}}^2, \tag{7}$$

where $P_{\mathrm{LM}} = T_1(\log t_1 + B_4)$, $T_1$ is the absolute temperature, $\sigma_1$ is the stress, $t_1$ is the time to 1 % creep strain, $B_1$ to $B_4$ are material constants.

Another quantity is the creep rate, which in alloys with low plasticity is characterized by minimum creep rate. By derivation of Eqs. (6a) to (6d) by time, one can obtain a creep rate curve, from which the minimum creep rate can be determined. In order to analyse the minimum creep rate as a function of temperature and stress, the model defined in [32, 33] was used in the form

$$\log \dot{\varepsilon} = C_1 + C_2 \log \left| \frac{1}{T} - \frac{1}{\mathrm{C}_5} \right| + C_3 \log \left[\sinh\left(\mathrm{C}_6 \sigma T\right)\right] + \\ + C_4 \log \left| \frac{1}{T} - \frac{1}{C_5} \right| \log \left[\sinh\left(C_6 \sigma T\right)\right], \tag{8}$$

where $\dot{\varepsilon}$ is the minimum creep rate (% $\mathrm{h}^{-1}$) and $C_1$ to $C_6$ are material constants.

#### 3.3.2. Analysis of creep characteristics

Creep characteristics were determined from creep deformation curves. The creep tests were carried out at applied stresses ranging from 80 to 540 MPa and temperatures from 750 to 975 °C. The time to fracture was measured to vary from 36 to 10495 h [34, 35]. Examples of some creep curves calculated according to Eq. (5) are presented in Fig. 4. It is possible

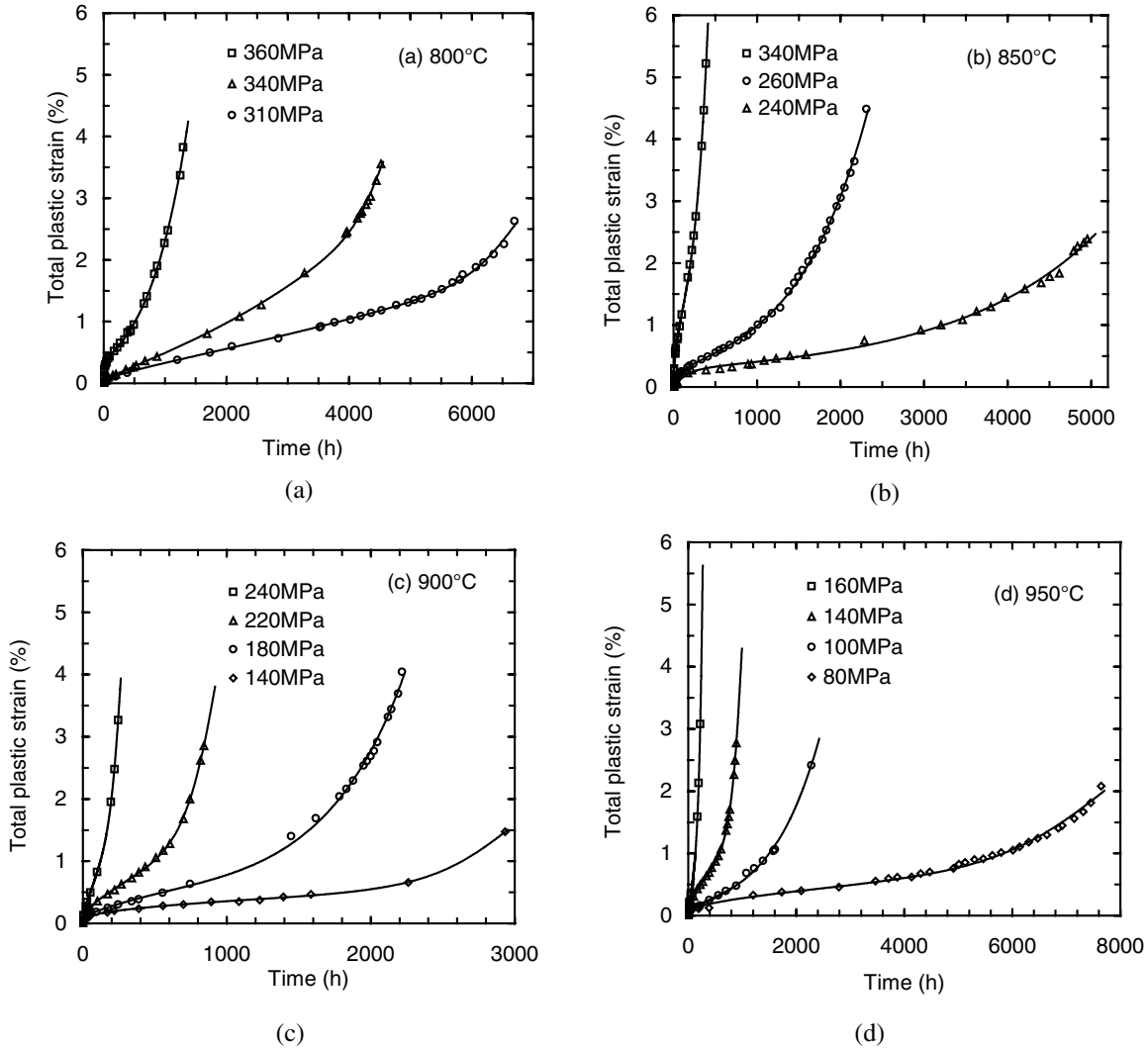


Fig. 4. Creep deformation curves showing dependence of total plastic strain on the time of nickel based superalloy IN 792 5A: (a) 800 °C; (b) 850 °C; (c) 900 °C; (d) 950 °C. The applied stresses are shown in the figures.

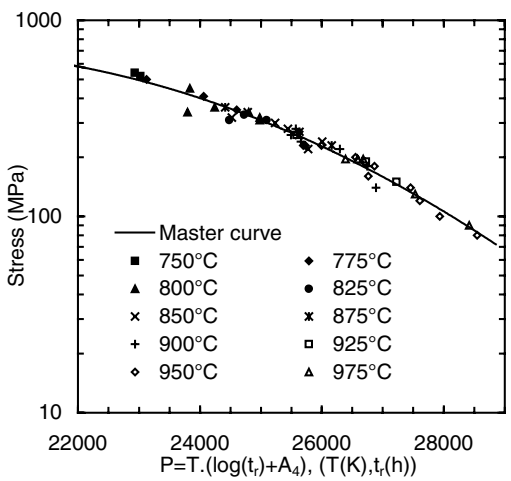


Fig. 5. Dependence of rupture stress on Larson-Miller parameter. The test temperatures are indicated in the figure.

to see that the fitting curves calculated using above described procedure have logical character, e.g. prolongation of creep life has tendency to decrease plastic strain.

Figure 5 shows rupture stress as a function of Larson-Miller parameter calculated from Eq. (3). Figure 6 illustrates the time to rupture as a function of stress and temperature. Corresponding constants of Eq. (3) are shown in Table 5. It is evident that the data for higher temperatures can be also very well fitted to time to rupture – stress curves.

Figure 7 shows stress for 1 % strain as a function of Larson-Miller parameter. Figure 8 shows dependence of time 1 % strain on stress at various temperatures. Material constants of Eq. (7) are shown in Table 5.

Figure 9 illustrates minimum creep rate as a function of stress at various creep temperatures. Calculated constants according to Eq. (8) are shown in

Table 5. Material parameters calculated from Eqs. (3), (7) and (8)

| Eq. (3) | | Eq. (7) | | Eq. (8) | |
|---|---|---|---|---|---|
| $A_1$ | $-1.08095721 \times 10^{0}$ | $B_1$ | $-2.32361121 \times 10^{-1}$ | $C_1$ | $-2.13513420 \times 10^{1}$ |
| $A_2$ | $4.09067706 \times 10^{-4}$ | $B_2$ | $2.78827287 \times 10^{-4}$ | $C_2$ | $-3.86464846 \times 10^{0}$ |
| $A_3$ | $-1.06479626 \times 10^{-8}$ | $B_3$ | $-6.23516284 \times 10^{-9}$ | $C_3$ | $-6.26871693 \times 10^{-1}$ |
| $A_4$ | $1.94516965 \times 10^{-1}$ | $B_4$ | $2.46893793 \times 10^{1}$ | $C_4$ | $-1.95308164 \times 10^{0}$ |
| Valid for $\sigma$ (MPa), $T$ (K), $t_r$ (h), $t_{1\%}$ (h) | | | | $C_5$ | $1.35048670 \times 10^{3}$ |
| | | | | $C_6$ | $6.20537446 \times 10^{-5}$ |
| | | | | Valid for (% $h^{-1}$), $\sigma$ (MPa), $T$ (K) | |

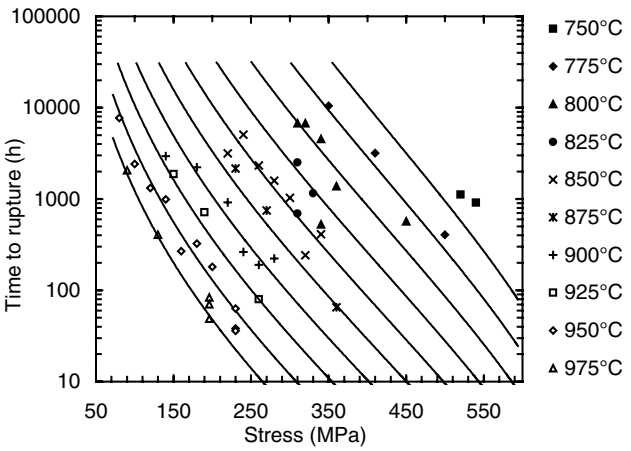


Fig. 6. Dependence of time to rupture on the stress for IN 792 5A superalloy. The test temperatures are indicated in the figure.

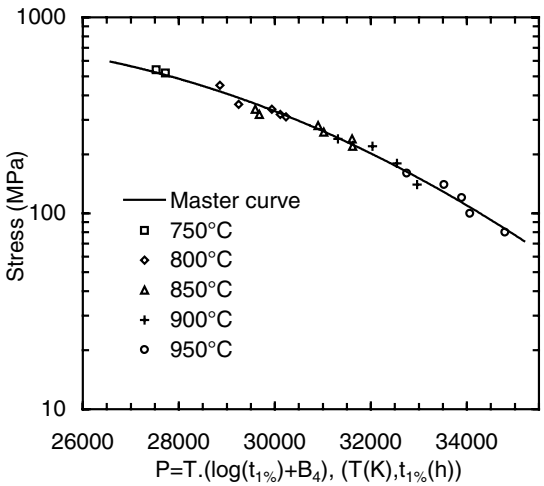


Fig. 7. Dependence of stress on Larson-Miller parameter for 1 % strain. The test temperatures are indicated in the figure.

Table 5. This data processing is very useful for calculation of long time service life.

### 3.4. Microstructure degradation during creep

Detailed microstructure evaluation was performed on two creep specimens subjected to long-term creep testing at 850 ℃/240 MPa for 5052 h and 950 ℃/80 MPa for 7704 h. Two main microstructure features were studied: (i) microstructure degradation during creep and (ii) creep fracture.

Detailed analysis of the crept specimens by SEM revealed that the initial cuboidal $\gamma/\gamma'$ microstructure is unstable during long-term creep exposure. Figure 10 shows the typical microstructure observed on longitudinal sections in gauge regions of the crept specimens. It is clear that some grains preserve nearly cuboidal $\gamma/\gamma'$ type of microstructure (Figs. 10a and 10c) but some exhibit well developed rafted type of microstructure (Figs. 10b and 10d). Three main features of rafted structure were statistically evaluated: (i) width of $\gamma'$ rafts, (ii) length of $\gamma'$ rafts and (iii) width of $\gamma$ channels separating the $\gamma'$ rafts. Each mean value of

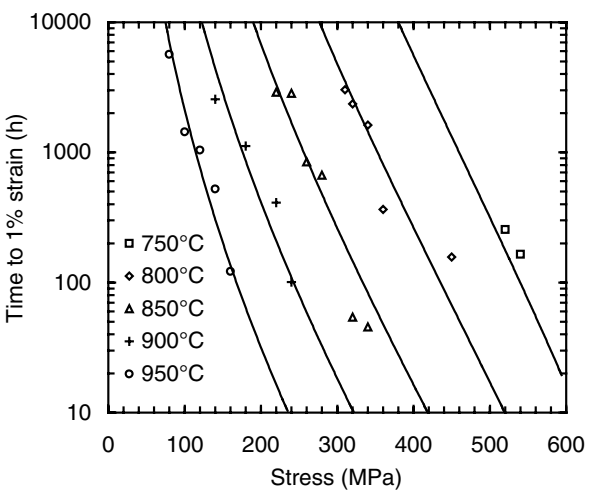


Fig. 8. Dependence of time for 1 % strain on the stress. The test temperatures are indicated in the figure.

the rafted structure was determined from log-normal distribution function. Figure 3 shows log-normal dis-

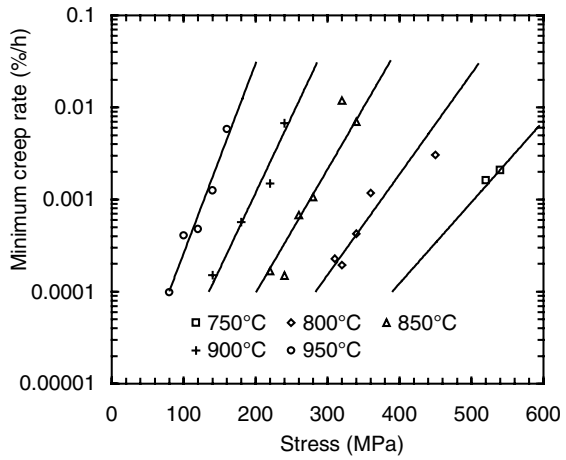


Fig. 9. Dependence of minimum creep rate on the stress. The test temperatures are indicated in the figure.

tribution curves of measured values of width of $\gamma$ channels in the studied crept specimens. The results of statistical quantitative image analysis of the grains, which showed minimum (coarsened cuboidal microstructure) and maximum (well developed rafted microstructure) degree of microstructure degradation within the gauge regions of the crept specimens, are summarized in Table 4. As it results from this table, the grains with minimum degradation after creep at 850 ℃ show bimodal distribution of $\gamma'$ precipitates. While the size of primary $\gamma'$ precipitates increases negligibly, the secondary precipitates underwent significant coarsening when compared to those in the specimens before creep testing. On the other hand, no bimodal distribution of $\gamma'$ precipitates is observed in the specimen after creep at 950 ℃ but the $\gamma'$ particles are significantly larger than those observed before creep. Increase of test temperature from 850 to 950 ℃ and creep time from 5052 to 7704 h results in well developed rafted microstructure, as seen in Table 4. The grains in the specimen crept at 850 ℃ show the early stages of rafting process. Significantly higher applied stress of 240 MPa at 850 ℃ is less effective to develop rafted microstructure than higher

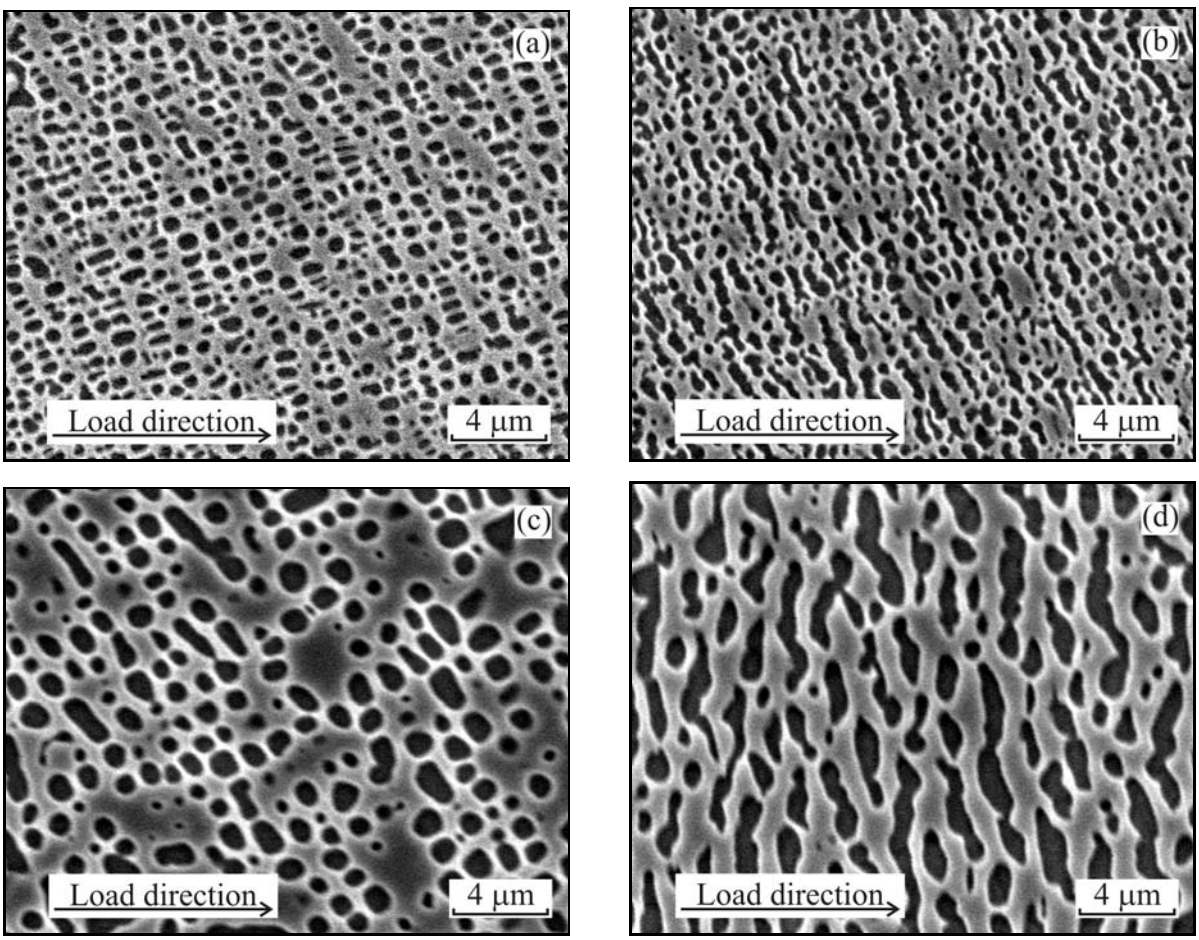


Fig. 10. SEM micrographs showing different level of microstructure degradation within individual equiaxed grains in the gauge region of creep specimens: (a) and (b) creep at 850 ℃/240 MPa for 5052 h; (c) and (d) creep at 950 ℃/80 MPa for 7704 h.

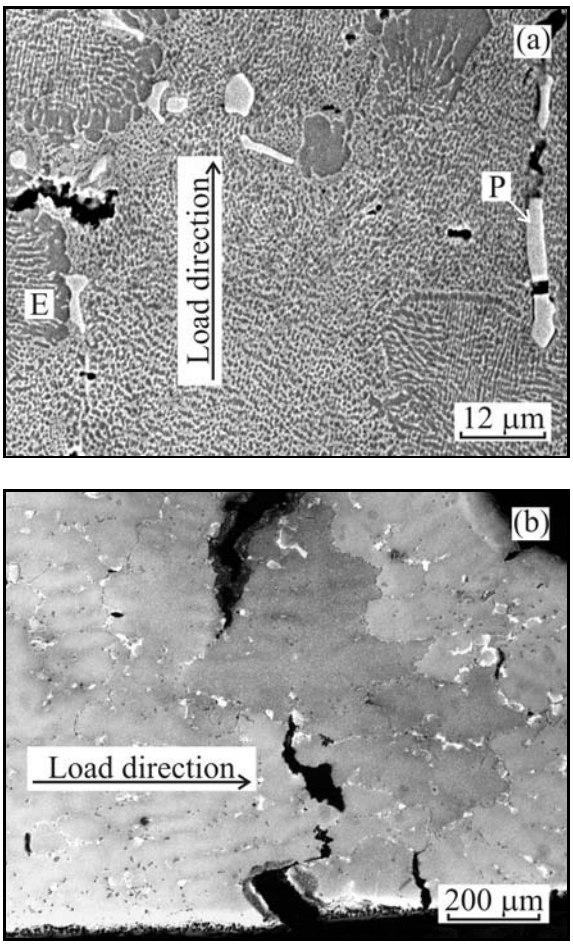


Fig. 11. (a) SEM micrograph showing cavities and cracks formed at interfaces between eutectic regions and the $\gamma/\gamma'$ matrix and around carbide particles; (b) LOM micrograph showing crack propagation along the grain boundaries. P – carbide particle, E – eutectic region.

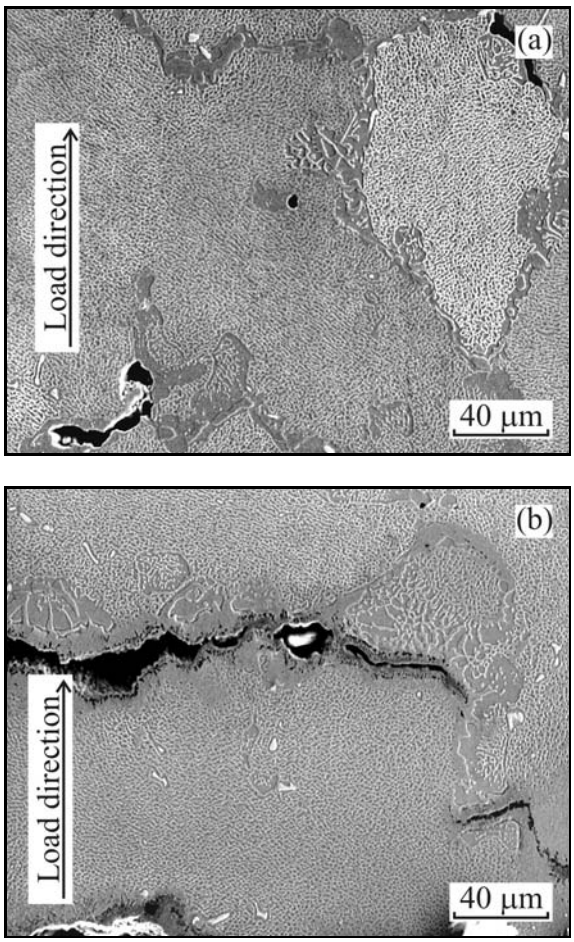


Fig. 12. SEM micrographs of the creep specimen tested at 950 °C/80 MPa: (a) coalesced cavities formed along the grain boundaries; (b) propagation of fracture crack along the grain boundaries.

test temperature of 950 °C and longer creep time of 7704 h.

### 3.5. Creep fracture mechanism

During the tertiary creep stage the studied creep specimens showed homogeneous plastic deformation within the gauge region with very limited local necking before fracture. Three main regions for nucleation of creep cavities and cracks were identified in the specimen crept at 850 °C/240 MPa: (i) grain boundaries, (ii) interfaces between eutectic regions and the $\gamma/\gamma'$ matrix and (iii) brittle carbide particles, as seen in Fig 11. Figure 11a shows cavities and cracks along the interface between eutectic regions and the matrix, cracking of brittle carbide particles and crack formation at interfaces between carbide particles and the matrix. As seen in Fig. 11b, the creep fracture of specimen is caused by coalescence of cavities and cracks formed along the equiaxed grain boundaries. Figure 12 shows fracture features of the specimen crept at 950 °C/80 MPa. No evidence for cracking of carbide particles or crack initiation along the carbide particle interfaces was found. The main mechanisms leading to fracture was diffusion controlled growth and coalescence of cavities along the grain boundaries, as seen in Figs. 12a and 12b.

## 4. Discussion

### 4.1. Creep performance of IN 792 5A

Figure 13 shows stress for 1 % strain for alloys IN 713 LC, IN 738 LC and IN 792 5A. The comparison was done using Eq. (3), for which a constant parameter of $A_4 = 21$ was chosen. The figure shows stress for 1 % strain for temperature 750 °C and life 1000 hours, and for 850 °C and 6000 hours. While the alloys IN 713 LC and IN 738 LC are very similar, the IN 792 5A clearly shows the highest stress values at identical

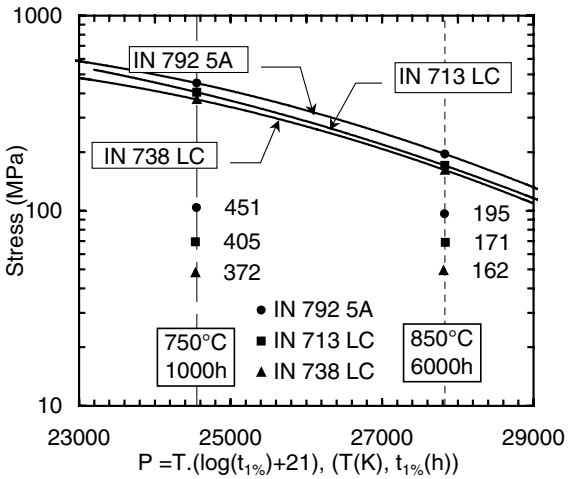


Fig. 13. Comparison of stress for 1 % creep strain of nickel based superalloys IN 792 5A, IN 738 LC and IN 713 LC.

Larson-Miller parameter $P_{\mathrm{LM}}$. The IN 713 LC is the longest used alloy by the industry. Its chemical composition is relatively simple and it is not prone to form $\sigma$ phase. This alloy has narrow solidification range and cast components can be used in as-cast state. There is no problem to achieve required creep properties using certified creep test procedure [36]. The IN 713 LC belongs to the first generation of Ni based superalloys. The IN 738 LC is the second generation alloy. Due to its complex alloying, it shows an increased resistance against sulphuric environment. It is about 50 % more expensive than the IN 713 LC. It is prone to form $\sigma$ phase during high temperature exposure. Hence, chemical composition of IN 738 LC must be optimized. In order to achieve required properties, the alloy has to be heat treated after casting. The IN 792 5A is also a material of high resistance against sulphuric environment. Its main advantage is that it has the highest high temperature strength from all assessed alloys. The same heat treatments have to be applied to IN 792 5A and IN 738 LC. However, the IN 792 5A is about three times more expensive than IN 713 LC.

### 4.2. Microstructure stability during creep

Detailed microstructure analysis of studied creep specimens showed no evidence for formation of $\sigma$ phase in the microstructure during long-term creep exposure. The metallographic observations are in agreement with calculations of electron vacancy number using PHACOMP method, which was lower than a critical value indicating no tendency of IN 792 5A to form the $\sigma$ phase.

As shown in Table 4, after creep testing at 950 ℃/80 MPa the creep specimen contained only one size distribution of $\gamma'$ precipitates. Fine secondary $\gamma'$ precipitates disappeared and primary precipitates underwent significant coarsening when compared to the initial microstructure. Since no interrupted creep tests were performed we can only speculate about the mechanisms controlling this process. We think that the primary precipitates probably grew on the expense of dissolution of unstable secondary precipitates. However, more complex mechanisms of particle coarsening can operate in the studied alloy. A similar change of bimodal type of microstructure and formation of one size distribution of $\gamma'$ particle was also observed by Wangayo et al. [4, 5] in a turbine blade made of nickel based superalloy Udimet 500 exposed to real operation conditions.

The development of rafted structure in single crystalline nickel based superalloys depends on crystallographic orientation to loading direction, lattice misfit, test temperature, applied stress and creep time [37, 38]. The lattice misfit $\delta$ is defined as the difference between the lattice parameter of the $\gamma'$ phase ($a_{\gamma'}$) and $\gamma$ phase ($a_{\gamma}$) by

$$\delta = \frac{2\,(a_{\gamma'} - a_{\gamma})}{a_{\gamma'} + a_{\gamma}}. \tag{9}$$

In the case of IN 792 5A, the lattice misfit is negative. Different degree of microstructure degradation of individual equiaxed grain in the studied alloy can be explained by their specific crystallographic orientation to tensile axis. As shown by Sass and Feller-Kniepmeier [37], while the creep specimens with crystallographic orientation [001] and [011] parallel to tensile axis showed microstructure rafting during creep, no rafting was observed in specimens with orientation [111]. No rafting can be explained by symmetrical coherency stress levels operating in the planes of the $\gamma/\gamma'$. On the other hand, rafting reduces different stress levels in the $\gamma$ matrix channels in the case [001] and [011] crystallographic orientation, which results in reduction of creep anisotropy for these orientations. It is clear that inhomogeneous rafting observed in the IN 792 5A can be well related to the various crystallographic orientation of individual grains.

## 5. Conclusions

The investigation of creep behaviour on the microstructure stability of cast nickel based superalloy IN 792 5A suggests the following conclusions:

1. The initial microstructure of the IN 792 5A alloy consists of cuboidal $\gamma'$ precipitates in the $\gamma$ matrix. Formation of carbide particles is observed in vicinity and along equiaxed grain boundaries. The $\gamma'$ precipitates show bimodal distribution before creep testing.

2. The methodology for evaluation of creep properties is described. Using this methodology, rupture

stress, stress for 1 % strain and minimum creep rates are determined from creep deformation curves.

3. Microstructural analysis of specimens subjected to long-term creep testing showed no evidence of $\sigma$ phase formation in the microstructure. These observations are in agreement with calculations of electron vacancy number using PHACOMP method, which showed that the alloy with the given chemical composition should not be pronounced to form the $\sigma$ phase.

4. During creep testing the microstructure degradation is observed. While some equiaxed grains still preserve cuboidal morphology of $\gamma'$ precipitates, formation of rafted structure was observed in other grains with suitable crystallographic orientation to loading axis. The size of coarsened $\gamma'$ precipitates, the width of $\gamma$ channels and length of $\gamma'$ rafts are determined quantitatively.

5. During the tertiary creep stage nucleation of cavities and cracks is identified at the grain boundaries, interfaces between eutectic regions and the $\gamma/\gamma'$ matrix and within brittle carbide particles. The specimens fail by the growth and coalescence of these cavities at low applied stresses and by coalescence of cavities and cracks formed along the brittle carbides at high applied stresses.

## Acknowledgements

This study was supported by the Ministry of Education, Youth and Sport of the Czech Republic – project VZ 257970001 and the Slovak Grant Agency for Science under the contract VEGA 2/70856/27. One of the authors (J. Lapin) expresses his thanks to MSc. T. Pelachová for kind assistance in metallographic analysis.

## References

[1] LUKÁŠ, P.—ČADEK, J.—KUNZ, L.—SVOBODA, M.—KLUSÁK, J.: Kovove Mater., *43*, 2005, p. 5.
[2] ROGANTE, M.—ŠAROUN, J.—STRUNZ, P.—CESCHINI, G. F.—RYUKHTIN, V.—LUKÁŠ, P.—MARINČÁK, V.: Kovove Mater., *43*, 2005, p. 371.
[3] ZRNÍK, J.—SEMEŇAK, J.—HORŇAK, P.—VRCHOVINSKÝ, V.: Kovove Mater., *43*, 2005, p. 93.
[4] WANGYAO, P.—ZRNÍK, J.—POLSILAPA, S.—NISARATANAPORN, E.—HOMKRAJAI, W.: In: Proc. Materials for Advanced Power Engineering 2006. Eds.: Lecomte-Beckers, J. et al. Jülich, Forschungszentrum Jülich GmbH 2006, p. 377.
[5] WANGYAO, P.—ZRNÍK, J.—MAMUZIC, I.—POLSILAPA, S.—KLAIJUMRANG, S.: Metallurgija, *46*, 2007, p. 195.
[6] KUNZ, L.—LUKÁŠ, P.—MINTÁCH, R.—HRBÁČEK, K.: Kovove Mater., *44*, 2006, p. 275.
[7] SCRIVANI, A.—RIZZI, G.—BARDI, U.: Kovove Mater., *43*, 2005, p. 382.
[8] SHAFRIK, R.—SPRAGUE, R.: Advanced Materials and Processes, *162*, 2004, No. 3, p. 33.
[9] SHAFRIK, R.—SPRAGUE, R.: Advanced Materials and Processes, *162*, 2004, No. 4, p. 27.
[10] SHAFRIK, R.—SPRAGUE, R.: Advanced Materials and Processes, *162*, 2004, No. 5, p. 29.
[11] WAHL, J. B.—HARRIS, K.: Superalloys in Industrial Gas Turbines – an Overview. In: Proc. 9th World Conference on Investment Casting. Paper No 9.12, San Francisco, West Bromwich, UK, CMF 1996.
[12] CHERUVU, N. S.—CHAN, K. S.—VISWANATHAN, R.: Energy Materials, *1*, 2006, p. 33.
[13] LAPIN, J.—BAJANA, O.: Kovove Mater., *43*, 2005, p. 169.
[14] LAPIN, J.—MAREČEK, J.—KURSA, M.: Kovove Mater., *44*, 2006, p. 1.
[15] LAPIN, J.: Kovove Mater., *43*, 2005, p. 81.
[16] LAPIN, J.—GABALCOVÁ, Z.—BAJANA, O.—DALOZ, D.: Kovove Mater., *44*, 2006, p. 297.
[17] LAPIN, J.: Kovove Mater., *44*, 2006, p. 57.
[18] ORLOVÁ, A.—KUCHAŘOVÁ, K.—DLOUHÝ, A.: Kovove Mater., *43*, 2005, p. 55.
[19] LAPIN, J.—PELACHOVÁ, T.—DOMÁNKOVÁ, M.—DALOZ, D: Kovove Mater., *44*, 2007, p. 121.
[20] PRAHL, J.—HAUŠILD, P.—KARLÍK, M.—CRENN, J. F.: Kovove Mater., *43*, 2005, p. 134.
[21] KRATOCHVÍL, P.—SCHINDLER, I.—HANUS, P.: Kovove Mater., *44*, 2006, p. 321.
[22] KRATOCHVÍL, P.—MÁLEK, P.—PEŠIČKA, J.—HAKL, J.—VLASÁK, T.—HANUS, P.: Kovove Mater., *44*, 2006, p. 185.
[23] PRAHL, J.—HAUŠILD, P.—KARLÍK, M.—CRENN, J. F.: Kovove Mater., *44*, 2006, p. 134.
[24] WAUDBY, P.: Ross and Catherall, UK, personal information.
[25] Metals Handbook. 9th edition. Ohio, ASM 1980.
[26] WOODYATT, R. L.—SIMS, C. T.—BEATTIE, H. J.: Trans. AIME, *236*, 1966, p. 519.
[27] SIMS, CH. T.: The Occurrence of Topologically Close-Packed Phases. The Superalloys. Eds.: Sims, CH. T., Hagen, W. G. N. York, J. Wiley Publ. 1972, p. 257.
[28] STICKLER, R.: Phase Stability in Superalloys. In: High-Temperature Materials in Gas Turbines. Eds.: Sahm, P. R., Speidel, M. O. Amsterdam, Elsevier 1974.
[29] HAKL, J.—VLASÁK, T.: Vývoj žárupevné Ni slitiny pro lopatky plynových turbin se zvýšenými požadavky na životnost a provozní spolehlivost. Výzkumná zpráva č. 03110011/a. Praha, SVÚM 2000.
[30] SEIFERT, W.—MELZER, B.: Rechnerische Auswertung von Zeitstandversuchen am Beispiel des Stahles 13CrMo4-4. 15. Vortragsveranstaltung Langzeitverhalten warmfester Stähle und Hochtemperaturwerkstoffe. Düsseldorf 1992.
[31] REKTORYS, K. a kol.: Přehled užité matematiky. Praha, SNTL 1981.
[32] BÍNA, V.—HAKL, J.: Mat. Sci. Eng. A, *234–236*, 1997, p. 583.
[33] PECH, R.—KOUCKÝ, J.—BÍNA, V.: Strojírenství, *29*, 1979, p. 389.
[34] HAKL, J.—VLASÁK, T.: Vyhodnocení výsledků creepových zkoušek slitin IN 713 LC, IN 738 LC a IN 792 5A. Výzkumná zpráva SVÚM, a. s., č. 2 31 0053/6. Praha 2004.

[35] HAKL, J.—VLASÁK, T.: Materiálové charakteristiky superslitin IN 713 LC, IN 738 LC, IN 792 5A, ŽS6W. Výzkumná zpráva SVÚM, a.s., č. 2 31 0053/7. Praha 2004.
[36] HAKL, J.—VLASÁK, T.—KOVAŘÍK. P.: Slévárenství, *LII*, 2004, p. 461.
[37] SASS, V.—FELLER-KNIEPMEIER, M.: Mater. Sci. Eng. A, *245*, 1998, p. 19.
[38] NABARRO, F. R. N.: Metall. Mater. Trans. A, *27A*, 1996, p. 513.